Nanoscale

COMMUNICATION

View Article Online
View Journal | View Issue

Check for updates

Cite this: *Nanoscale*, 2024, **16**, 61

Received 2nd October 2023,
Accepted 4th December 2023

DOI: 10.1039/d3nr04961b

rsc.li/nanoscale

Detection of medically relevant volatile organic compounds with graphene field-effect transistors and separated by low-frequency spectral and time signatures†

Bruno Gil, * Dominic Wales, Haijie Tan and Eric Yeatman

Exhaled human breath contains a mixture of gases including nitrogen, oxygen, carbon dioxide, water vapour and low molecular weight volatile organic compounds (VOCs). Different VOCs detected in human breath condensate have been recently related to several metabolic processes occurring inside body tissues in the pathological state, as candidate biomarkers for monitoring conditions such as lung injury, airway inflammation, immunity dysfunction, infection, and cancer. Current techniques for detecting these compounds include several types of mass spectroscopy, which are highly costly, time-consuming and dependent on trained personnel for sample analysis. The need for fast and label-free biosensors is paving the way towards the design of novel and portable electronic devices for point-of-care diagnosis with VOCs such as E-noses, and based on the measurement of signal signatures derived from their chemical composition. In this paper, we propose a device for VOC detection that was tested inside a controlled gas flow setup, resorting to graphene field-effect transistors (GFETs). Electrical measurements from graphene directly exposed to nitrogen plus VOC vapours involved cyclic measurements for the variation of graphene's resistance and low-frequency spectral noise in order to obtain distinctive signatures of the tested compounds in the time and frequency domains related, respectively, to Gutmann's theory for donor–acceptor chemical species and spectral sub-band analysis.

Introduction

Graphene, as a one atom thick layer of carbon material, has been extensively used in the past years as a primal candidate for sensing molecular-level interactions with gas, liquid and solid (dielectric) materials, due to its superior electrical, optical, mechanical, and physical properties.[1–4] In medical healthcare applications, graphene has been regarded as a material that offers both biocompatibility and high stability to surrounding body tissues owing to its hydrophobicity and chemically inert structure. Although graphene can be employed as a 2D material for the realization of biosensing electrodes, surface coatings or membranes,[5,6] one of its major applications comes in the form of graphene field-effect transistor (GFET) technology, in which a graphene monolayer is surrounded by metal pads composing the drain and source regions of the transistor and deposited on top of silicon dioxide (SiO_2) and silicon (Si) layers. An additional metal pad for the transistor gate is then placed either near the graphene layer but without physical connection creating the so-called top-gated GFET or below the Si substrate to yield back-gated GFETs.[1,7] In any of the approaches, the transistor structure can be highly miniaturized and designed with multiple individual units, which are compatible with standard CMOS fabrication processes, attractive aspects for the creation of the next generation of high-performance electronic devices.[8] Graphene can alter its electronic band structure due to the adsorption of dopant atoms at the surface, thus creating a non-zero bandgap that is highly desirable in digital electronic applications, whereas graphene's conduction of both electrons and holes with high mobility and tunable conductivity creates an unparalleled "ambipolar electric field behaviour" as a function of the applied gate voltage that can be further explored for sensing electronics.[9–12]

In the medical field, GFET sensors or devices have already permitted the monitoring of disease biomarkers in cancer,[3,13,14] as well as respiratory, immunologic, neurodegenerative,[6,15] cancer[16] and infectious[17] conditions due in part to the ability of immobilizing antibodies, aptamers, or other molecules at the surface of graphene that bind to specific biological targets. However, functionalization of graphene with ligand molecules can involve multiple chemical steps that are both laborious and time-consuming, without the guarantee that non-specific adsorption of contaminant molecules will degrade sensor performance, or worse, destroy the graphene layer and associated materials, therefore making it impossible to re-use the sensing unit, especially in electrolyte-

---

Department of Electrical and Electronic Engineering, Imperial College London, South Kensington Campus, London SW7 2AZ, UK. E-mail: b.gil-rosa@imperial.ac.uk

† Electronic supplementary information (ESI) available. See DOI: **https://doi.org/10.1039/d3nr04961b**

based GFETs. Liquid and solid materials can damage the structure of graphene during intense testing, from which graphene cannot completely recover its initial properties, even upon exposure to vacuum, UV light or other washing chemicals, thus leaving only gas or wireless stimulation (by light, ultrasound or radiofrequency) as the available options that produce unscathed effects on the surface of graphene within reasonable limits.[18,19]

Recently, GFET sensors have been considered as potential candidates for the design of electronic nose (E-nose) devices that specifically target the monitoring of bodily gases to determine their chemical composition, associated exposure risks, and potential pathological implications on the health of an individual.[20] Volatile organic compounds (VOCs) fit within this category as a class of heterogeneous groups of carbon-based chemicals characterized by high mobility and volatility at ambient temperature with the ability to permeate biological membranes and cross the blood–brain barrier.[21] VOCs can originate externally from ambient sources and enter the body through dermal contact, ingestion and inhalation processes or they can be the result of internal metabolic processes occurring inside body tissues in the pathological state, with traces of some VOCs being detected in human breath condensate, blood, faeces, and urine.

From the different types and sources of volatile organic compounds discussed previously, the ones contained in exhaled human breath are the sole targets of the current study. In this regard, exhaled breath can be viewed as a mixture of different gases such as nitrogen, oxygen, carbon dioxide, water vapour and other inert gases, alongside many low molecular weight VOCs.[20] These have the potential to provide information about lungs' functioning (and associated organs through systemic circulation: heart, liver, and breast), lung injury, airway inflammation, immunity dysfunction, cancer, and neurological disorders. Examples of breath VOCs recently classified as biomarkers for some medical conditions include 1-propanol, which has been found in patients with pneumonia (biomarker of bacterial growth); pentane and methanol in cystic fibrosis infection by *P. aeruginosa*; ethanol and butane in *H. pylori* infection and tuberculosis;[22] limonene in patients with liver cirrhosis or hepatic encephalopathy;[21] cyclohexanone and 2-butanone reported in airway inflammation and asthma;[23] acetaldehyde for acute respiratory distress syndrome;[20,22] pentane and 2-methylpentane in lung cancer; acetone in the diagnosis of diabetes mellitus and ketonemia; isoprene in renal disorders; isoprene and ethanol in chronic kidney disease;[24] isoprene and acetonitrile in head–neck cancer patients; styrene and decane in hepatocellular carcinoma;[25] or, more recently, ethanol, acetone, butanone and methanol in the viral infection by SARS-Cov-2.[22]

Current technologies employed to detect breath VOCs include gas-chromatography mass spectroscopy, proton transfer reaction mass spectroscopy and ion-mobility mass spectroscopy, which separate compounds with high specificity and reproducibility, though the associated costs incurred by such techniques are hugely high due not only to the sophisticated laboratory equipment employed but also to the expenses from sample collection, preparation, storage and processing by specialized personnel, thus leading to laborious and prolonged analysis times.[26] The recent trends in label-free biosensor development, miniaturization, remote deployment (that is, outside laboratory conditions) and connection to the Internet of Healthcare Things, such as E-nose devices,[21,27] may provide a fast and less expensive alternative to surpass the above shortcomings in VOC detection while recognizing and classifying different compounds through a comparison with pre-programmed patterns or breath "signatures" after the conversion of chemical information convoyed by the VOCs into electrical signals, vibrations or fluorescence traces.[26–28] Nonetheless, the stability of such sensors and their sensitivity, specificity and reliability overtime are still debatable, which has slowed down their translation into real clinical applications in the form of point-of-care diagnostic or wearable devices.

In this paper, we employed unfunctionalized GFETs to measure the change in graphene's resistance and $1/f$ noise metrics when subjected to a constant flow of VOC vapours and transported by nitrogen gas inside a controlled experimental setup, as shown in Fig. 1. To achieve this, a custom-made electronic readout device was developed with multiplexing capability to address 12 independent graphene sensing units (or channels) and increase the statistical significance of the measured signals, while allowing different measurement modalities to be tested, namely, time measurements of DC resistance, AC impedance and low-frequency spectral noise.[29] Finally, digital processing of the acquired signals by means of a filter bank was performed to help identify spectral signatures of the tested compounds, alongside Gutmann's theory for donor–acceptor species in interaction with graphene.[30,31] Previous research studies on the topic of VOC detection with GFETs have used functionalized graphene to target individual compounds.[32–37] Although this approach yields higher specificity towards the selected VOC, it cannot be applied to a different compound with similar performance metrics. Due to the heterogeneous composition of most biological fluids and exhaled condensate in terms of VOC content (that is, many VOCs reported for the same medical condition as previously mentioned), we believe that a universal graphene template must be deployed without specifically targeting single compounds by chemical functionalization; instead it must provide identical physical interaction with a larger group of compounds, from which characteristic physical signatures can be identified by different measurement modalities and relative to a common baseline, such as (inert) nitrogen gas.

Materials and methods

GFET chip array technology

A commercially available S-20 GFET chip array was purchased from Graphenea (Spain), containing 12 graphene channels disposed along the central area of the chip (1 cm^2) and on top of

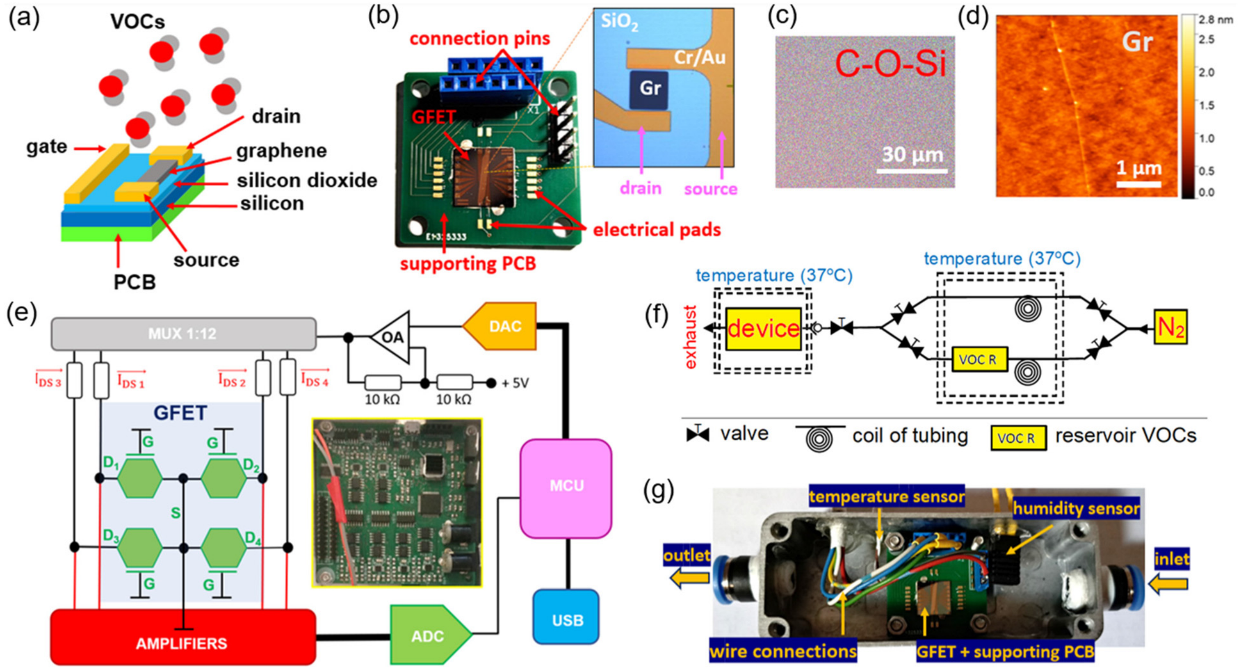

Fig. 1 (a) Contextualization image for the detection of volatile organic compounds with graphene field-effect transistors. (b) GFET chip array attached to the supporting PCB for external electronic signal access and microscopic image of a single graphene channel (inset) with composing materials. (c) EDX image of the graphene channel revealing a uniform distribution of the carbon (C), oxygen (O) and silicon (Si) elements. (d) Surface thickness of the graphene channel obtained by atomic force microscopy (AFM). (e) Simplified schematic for the electronic readout device developed to interface the GFET chip array. (f) Gas flow apparatus built to provide a controlled setup for exposure to the graphene device. (g) Enclosed metal box containing the GFET chip array for VOC vapour sensing, as well as internal sensors for control of temperature and humidity parameters during the experiment.

SiO_2 (thickness of 90 nm) and Si layers (675 µm), as depicted in Fig. 1b. A monolayer graphene sheet was produced by chemical vapour deposition (CVD) on a copper catalyst according to the specifications of the manufacturer and transferred to the chip by a wet transfer process, yielding a uniform distribution of carbon, oxygen and silicon elements along the channel (Fig. 1c and S1 in the ESI†), a graphene thickness of ≈0.5 nm with 97% transparency, and Raman peak ratios of $I(D)/I(G) < 0.1$ and $I(G)/I(2D) < 1$ (Fig. 1d). Each monolayer of the graphene film for the 12 channels (dimensions: 90 µm × 90 µm) was layered on top of metal pads for the drain and source electrodes made from a 50 nm thick Cr/Au material. An encapsulation layer (50 nm Al_2O_3 + 100 nm Si_3N_4) was deposited to protect the contact surface between the graphene channels and respective metal pads to avoid passivation of the entire chip, whereas the central area of the channels was left exposed for contact with gas molecules. By its turn, a single large metal pad for the gate electrode was deposited over the SiO_2 layer, running along its entire central extension. The end terminations of each metal pad (drain, source, and gate) located at the edge of the chip array were wire-bonded to a supporting printed circuit board (PCB) using a TPT HB wire bonder machine with a 50 µm thick Au wire. Electrical performance metrics obtained from the combination of this GFET chip array and a readout system (to be introduced in the following sections) have shown similarities to the curves provided by the manufacturer, namely the typical I_{DS}–V_{DS} linear profile and the transfer curve (R_{DS}–V_{GS}), the latter measured in PBS solution (thus yielding an electrolyte-based GFET sensing unit with top-gating[4,16]).

Supporting PCB for GFET testing in gas experiments

A double layered PCB with planar dimensions of 2 cm × 2 cm and a thickness of 1.55 mm was designed using Eagle software (Autodesk Inc., USA) to support the GFET chip array during the VOC experiments and fabricated with standard FR4 materials. Small electronic pads (1 mm × 1 mm) were placed along the sides of the GFET chip array for wire-bonding purposes, with copper traces (width of 0.1 mm) connecting these pads to connection pins located at the edge of the PCB for external signal access and disposed in a way to avoid crossing underneath the area occupied by the silicon substrate from the chip array. The exposed pads for wire bonding and external connections were covered by a Ni/Au surface finishing process over the copper traces, whereas the remaining areas of the PCB were covered by a liquid photo-imageable solder mask to which adhesive tape was attached to hold the GFET chip array.

Electronic readout device for GFET characterization

The electronic readout device for electrical measurements with the GFET chip array consisted of a single double-layered PCB fabricated with the same technology as the previous supporting PCB and populated by off-the-shelf electronic components on the top layer only, which impose user-selectable voltage levels to the drain–source (V_{DS}) and gate–source (V_{GS}) electrodes, as schematically represented in Fig. 1e. Voltage signals were then imposed over the available graphene channels on a time multiplexed way (MUX) and generated by a digital-to-analogue converter (DAC) embedded inside electronics that transforms digital samples stored inside the central microcontroller (MCU) into an analogue equivalent in terms of the waveform profile for the measurement modalities of AC impedance and spectral noise (a bandwidth of 15 kHz, a voltage resolution of 0.25 mV, ±5 V range) or the constant level for the DC regime, followed by signal filtering and conditioning before injection into the individual graphene channels. On the other electronic side, the drain–source current (I_{DS}) flowing through the graphene channels was amplified and detected by independent acquisition channels before digitization using an analogue-to-digital converter (ADC) at a rate of 50 kSPS and a resolution of 20 nA. These data samples were afterwards sent to a computer through USB communication where the final value for I_{DS} (or its inverse, the resistance R_{DS}) was estimated in the DC and AC regimes (Fourier transform), as well as for the spectral noise (filter bank), depending upon the selected measurement modality inside a graphical user interface developed in Matlab (Mathworks Inc., USA).

Experimental setup devised for gas sensing with GFETs

The setup for the gas sensing experiments in Fig. 1f included a gas source (nitrogen bottle, N_2, flow rate set between 0.5 and 5 l min^{-1}) from which two different pipelines carry the inert gas to a heated reservoir at 37 °C, with one of the line branches passing through a condenser where N_2 is mixed with the vapours from the selected VOC (and contained in a separate reservoir) by heating a liquid solution with the same chemical composition. Then, two opposing non-return valves select the type of gas (pure N_2 flow or N_2 plus VOC vapour) flowing inside a second enclosed metal chamber where the GFET chip array is located. Temperature and humidity sensors were also added to the chamber to measure these two physical properties as gas is flowing through the chamber, with data readings being obtained by external commercial equipment using access wires passing through the walls of the chamber, including those involved in connecting the GFET chip array to the electronic readout device. Both access wires were air-tight sealed to the external surface of the metal enclosure at specific points located sideways relative to the GFET chip array (Fig. 1g). This setup serves two purposes: (1) on the one hand, a clean and prolonged flow of nitrogen gas allows to reset the electrical properties of graphene after exposure to a particular VOC, while expelling any remnants of the compound through an escape valve or by introducing vacuum to the chamber and (2) on the other hand, it permits cyclic resistance measurements of graphene between periods of pure N_2 flow and periods of N_2 plus VOCs. Finally, liquid solutions with a similar chemical composition to the targeted VOCs in the current study were purchased directly from Sigma Aldrich (USA) and Merck (Germany) suppliers.

Results and discussion

Characterization of the graphene layer involved Raman spectroscopy using a DXRTM2xi Raman microscope (Thermo Fisher Scientific Inc., USA) with a 50× long distance objective lens and the following settings: 532 nm excitation, 0.5 mW laser power, 50 Hz exposure and 0.2 s acquisition time. The measured spectrum is show in Fig. 2a, where the graphene peaks were identified at around 1380 cm^{-1}, 1600 cm^{-1} and 2700 cm^{-1} for the D, G and 2D bands, respectively.

Electrical characterization of the graphene channels within the GFET chip array under open-air conditions was performed by measuring the I_{DS} current while sweeping the voltage level on the V_{DS} signal from −0.2 V to 0.2 V in incremental steps of 0.01 V (DC regime, V_{GS} = 0 V), and the general profile as shown in Fig. 2b was obtained. The average maximum I_{DS} current measured for the 12 graphene channels included on the GFET chip array was around 150 μA (V_{DS} = 0.2 V), with a slope of 750 μA V^{-1}. Statistical metrics – average and standard deviations – for the electrical signals measured by the 12 graphene channels available on the system are shown in Fig. S2a of the ESI,† which show small deviations from the average metric measured, and so from this point of view, the obtained results are ascribed to an average value calculated amongst the 12 channels. In this regard, Fig. 2c shows the AC impedance curve in the range between 1.250 kHz and 10 kHz, with an increasing amplitude profile up to the middle of the spectrum, which begins to decrease slightly for the higher frequencies tested, revealing a mixture of inductive and capacitive behaviours in the description of the electrical model for graphene, although the decrease in amplitude due to the capacitance is smaller (≈5 Ω) as compared to the increase in amplitude from the inductive part of the spectrum (≈15 Ω), therefore predominant in the electrical model of graphene with a positive amplitude slope of 2.6 mΩ Hz^{-1} between 1.250 kHz and 6.250 kHz and a negative slope of 1 mΩ Hz^{-1} for the remaining spectrum. For the spectral noise exhibited in Fig. 2d, it presents the typical 1/*f* curve profile expected for graphene, with about one order of magnitude decrease per decade of frequency increase (from 10 Hz to 500 Hz), whereas closer to the DC point (from 1 Hz to 10 Hz), the spectral noise deviates slightly from the 1/*f* curve, decreasing in magnitude. Reasons for this behaviour might be related to the influence of surrounding equipment operating closer to the readout device (namely, gas and vacuum pumps).

In what concerns the gas experiments, at the beginning of each recording, we decided to allow some time for the resistance curve of graphene to reach a stable value (Fig. 2e), a process also called "Joule heating", in which the I_{DS} current flows through different graphene channels (DC mode, V_{DS} = 0.2 V, V_{GS} = 0 V), thereby raising the local temperature from the initial state of graphene. This helps stabilizing the behaviour of charges along the graphene channel. We found that roughly 600 s (10 min) of exposure to Joule heating was required to stabilize the R_{DS} baseline before nitrogen gas injection. The Joule heating process is related to the DC resistance

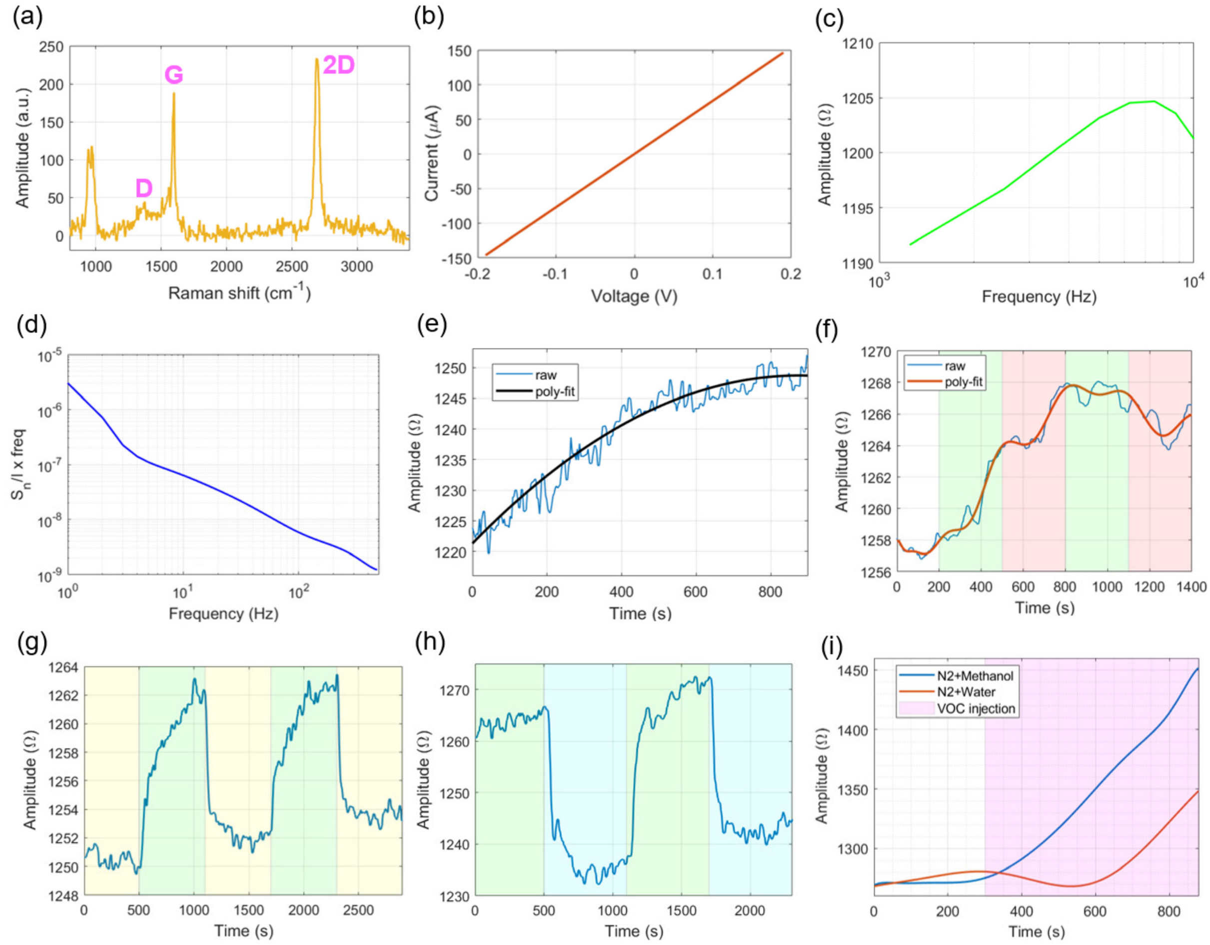

Fig. 2 (a) Raman spectra and the corresponding graphene bands (D, G and 2D). (b) I_{DS}–V_{DS} curve obtained for the graphene channel under the open-air conditions. (c) AC impedance of the graphene channel under the same conditions. (d) Respective low-frequency spectral noise. (e) DC resistance of graphene as a function of time during the Joule heating procedure (signal stabilization). (f) Variation of the resistance of graphene upon exposure to different flows of nitrogen (green shade: 1 L min^{-1}, red shade: 0.5 L min^{-1}). (g) Measurements of the graphene resistance upon cyclic exposure to vacuum (yellow shades) and nitrogen (1 L min^{-1}, green shades). (h) Cyclic resistance measurements for graphene exposed to nitrogen (green shades) and nitrogen plus water vapour (blue shades). (i) Resistance profiles for the injection of VOC vapours from methanol (blue line) and water (orange line) during excess temperature rise.

offered by the graphene channel when stimulated by V_{DS}. Since impurities adsorbing to the surface of graphene have been removed during the cleaning process (pure N_2 flow and vacuum) and the resistance offered by metal contacts and wire cables in the GFET structure is minimal (as measured using a spectrum analyzer – model E4990A, Keysight, USA – with values of 1.3 ± 0.3 Ω and 0.8 ± 0.2 Ω, respectively, for the bandwidth between DC and 10 kHz), only the graphene material can contribute considerably for the DC resistance offered for I_{DS} current circulation. As the Joule heating is determined by the DC resistive behaviour of materials ($W = V_{DS}I_{DS} = I_{DS}{}^2R_{DS}$, where W is the dissipated Joule power[38]), this effect can be better visualized in materials whose resistive behaviour is easily influenced by constant current circulation until reaching stabilization (like graphene), as opposed to pure resistive materials, whose conductivity is independent of exposure time at a constant DC voltage.

For the flow of nitrogen gas, we experimented with different rates (from 0.5 L min^{-1} to 1 L min^{-1}), and thus obtained the resistance profile as shown in Fig. 2f. The initial flow rate of 1 L min^{-1} for N_2 produced a change of resistance $\Delta R_{DS} \approx 6\ \Omega$ during the initial 300 s of injection (and translated into a rate of 20 mΩ s^{-1}), whereas a flow of 0.5 L min^{-1} resulted in slightly half of that amount. Curiously, after the first cycle of N_2 flow rate variation, the second injection of N_2 at a rate of 1 L min^{-1} did not contribute to the increase in graphene's resistance, instead producing an overall downward trend, which is further enhanced by reducing the flow rate back to 0.5 L min^{-1}. We postulate that this behaviour is related to physical adsorption and desorption phenomena occurring between the nitrogen molecules and the surface of graphene: a disturbance to the original flow rate (that is, from 1 L min^{-1} to 0.5 L min^{-1}) induces an imbalance to the original system's thermodynamics (physisorption potential) that ultimately alters the resistance of graphene. However, after vacuum cleaning of the GFET chamber and restoration of the electrical properties for graphene, the trend of resistance variation for the flow of nitrogen at 1 L min^{-1} is again recovered. Given these observations, for the subsequent experiments, we decided to fix the flow rate of N_2 to 1 L min^{-1} to rule out the influence of different flow rates in R_{DS}.

Similarly, we tested the influence of vacuum injection in the resistance value of graphene in-between cycles of nitrogen flow (1 L min^{-1}). From Fig. 2g, it can be seen that the vacuum has an effect of lowering graphene's resistance back to a stable baseline level ($\Delta R_{DS} \approx 10\ \Omega$), while N_2 injection causes a resistance increase that takes a longer time to stabilize. Therefore, injection of vacuum through the device chamber can be explored to reset the electrical properties of graphene to an initial state, explained electrochemically by the removal of absorbed molecules to the surface of graphene. For the experiments with VOC vapours, we started by using deionized water as the heated liquid (37 °C) inside the reservoir, with the produced vapours transported by N_2. Fig. 2h shows cyclic resistance measurements performed by switching between periods of pure N_2 flow and N_2 plus water vapour, with the latter producing a decrease of ≈25 Ω in the baseline R_{DS} value. By increasing the heating temperature (50 °C) of the respective VOC-containing liquid inside the reservoir, we observed an exponential increase of the measured resistance, not only for the water vapour (Fig. 2i, which contradicts the previous decrease in R_{DS}), but also for methanol vapours, when inserted on the setup, the latter producing even larger increases in resistance. To rule out the influence of temperature rise in the electronic readout measurements, we performed a similar test but without gas flow passing through the GFET chamber, and thus obtained a lower R_{DS} value increase (≈20 Ω, Fig. S2b†). The effect of sudden temperature rise during gas flow not only increases the R_{DS} value, but also the vapour pressure of the VOC inside the chamber, which contributes to the deposition of moisture over the surface of graphene, as detected by the humidity sensor. Since methanol is a more volatile species than water, more vapour molecules of methanol are dispersed and interact with the structure of graphene, thereby influencing the flow of charges within its channel. To avoid the formation of VOC moistures inside the device chamber, we decided to uniformize the temperature distribution (37 °C) along the different parts of the gas exchange setup and, thus avoid large temperature gradients between the (heated) source of VOCs and the GFET device located further down on the pipeline. Moreover, for a real application as a medical device, the temperature and/or other physical variables (*e.g.*, intrabody pressures, fluid velocities, *etc.*) will not deviate dramatically from homeostasis levels, which validates our assumption of keeping physical variables such as temperature and gas flow rates within physiological limits.

Fig. 3a shows the 16 VOCs tested during gas sensing arranged into 6 different groups according to chemical structure similarities, from which some representative signal traces will be shown throughout the rest of the manuscript. Cyclic resistance measurements are depicted in Fig. 3b for some VOC vapours including methanol, heptane, decane, tetrahydrofuran (THF) and dichloromethane. From the displayed curves, it is worth noting that while methanol, decane and dichloromethane show decreased R_{DS} values relative to that of pure N_2 flow, THF exhibits a different trend (R_{DS} increase) while heptane shows no significant resistance changes. Furthermore, methanol, decane and THF yielded more pronounced trace transitions between cycles than dichloromethane and heptane. Regarding the latter, the fact that there are no abrupt transitions for R_{DS} make us assume that, due to the molecular structure and comparable number of carbon atoms, the interaction between graphene and heptane produces fewer signal variations (due to similar electronegativity), as opposed when in the presence of polar structures such as –OH and –Cl groups. In addition, the fact that decane (10 carbon atoms) already produces considerable signal changes in graphene, contributing to a resistance variation that is dependent on the (heavy) number of carbon atoms present in the interaction. The complete R_{DS} transition (or step) from pure N_2 flow to N_2 plus tested VOCs is shown in Fig. 3c, occurring around 300 s into the recordings, in which the traces have also been subtracted from the baseline nitrogen level (Fig. S2c†) to yield the change on graphene's resistance overtime (ΔR_{DS}) solely due to VOC circulation. While *N*-methyl-2-pyrrolidone (NMP), THF and acetone vapours produce positive ΔR_{DS} shifts, the remaining tested VOCs induce negative ΔR_{DS} changes (relative to pure N_2 flow), with the sole exception occurring for heptane that produces insignificant ΔR_{DS} variations. The magnitude for ΔR_{DS} also varies according to the tested VOC, which can potentially be explored to identify the compound in accordance with Gutmann's theory for donor–acceptor species.[30,31] The difference between the donor and acceptor numbers, DN and AN, respectively, indicates the overall tendency for a solvent to donate or accept electrons which, inevitably, alter the interaction with graphene. In Table 1, we observed that VOCs with a positive ΔR_{DS} have a positive DN − AN metric, with negative metrics yielding a negative ΔR_{DS}. From the available classification of the different compounds according to Gutmann's theory, we observed almost a 100% correspondence with the results obtained in Fig. 3c, the only exception being diethyl ether, though the following two factors can be accounted for this small discrepancy: (1) the boiling point of diethyl ether is closer to the setup temperature than any other tested compounds (34.6 °C) and (2) the metrics for ΔR_{DS} and $\Delta R_{DS}/\Delta t$ are the lowest values recorded for (neutral) heptane.

We also observed that the magnitude of the DN − AN metric in the table does not translate into a proportional magnitude for ΔR_{DS}, with some compounds such as water (DN − AN = −36.8) yielding a lower ΔR_{DS} value relative to that of chloroform (DN − AN = −19.1). One explanation for this behaviour can be attributed to the fact that these two compounds have different vapour pressures at 37 °C (V_P [water] < V_P [chloroform]), which prevents higher resistance signal excursions beyond the levels detected by the proposed GFET system

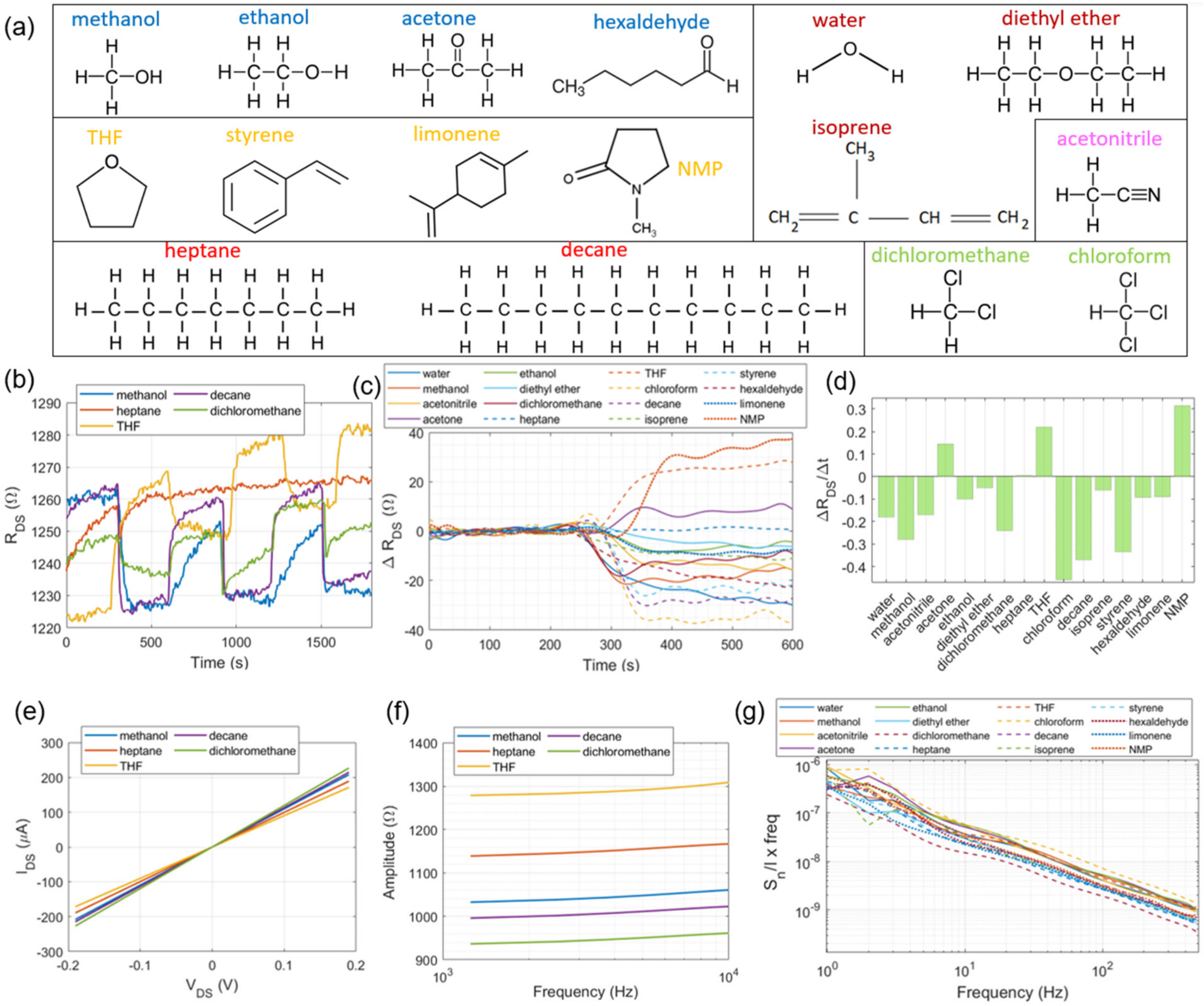

Fig. 3 (a) Volatile organic compounds tested in the experiment and divided into 6 groups according to the chemical structure. (b) Cyclic time measurements obtained for the graphene's resistance when exposed to nitrogen (300 s) and nitrogen plus VOC vapours (300 s). (c) Variation of the resistance value on the transition between nitrogen exposure and nitrogen plus VOCs (step transition occurs at 300 s). (d) Respective slope for the variation of graphene's resistance overtime ($\Delta R_{DS}/\Delta t$) obtained for the tested VOCs. (e) I_{DS}–V_{DS} profiles obtained for 5 different VOCs (V_{GS} = 0 V). (f) Respective AC impedance curves in the range between 1.25 kHz and 10 kHz. (g) Low-frequency spectral noise measured for all the tested VOCs.

if vapour pressures from the different VOCs were to be equalized at the same level as in ref. 19, surpassing the safe physiological limits. Nonetheless, the qualitative separation of compounds in terms of donor–acceptor species still stands for the conditions of the experimental setup. Another reason might be related to the fact that some of the detected resistance traces do not completely stabilize within the time allowed for cyclic measurements (300 s), which produces fluctuations on the traces. By measuring other signal metrics such as the ratio $\Delta R_{DS}/\Delta t$ calculated over the transitional step (that is, ΔR_{DS}: the amplitude level variation in-between the end of nitrogen injection and the beginning of VOC circulation until the latter reaches a first stable value or flat profile; Δt: the precise amount of time that is required to obtain this first slope – in the range of $\in[300–350]$ s – before additional curve excursions over the ΔR_{DS} trace), we obtained the bar plot in Fig. 3d that allows to distinguish among some VOCs whose ΔR_{DS} traces overlap towards the end in Fig. 3c, such as dichloromethane and acetonitrile.

Measurement of the graphene channel resistances in DC (or inverse, I_{DS}) and AC modes for five exemplary VOCs is depicted in Fig. 3e and f, respectively. While the I_{DS}–V_{DS} curve (step of 5 mV) might still be enough to differentiate between the VOCs for the larger V_{DS} levels imposed, the AC impedance curves provide an even clearer curve separation amongst the VOCs, a fact that can be attributed to the differential interactions in terms of specific sub-bands between graphene and the chemical composition of the VOCs. In fact, the low-frequency spectral noise curves depicted in Fig. 3g for all the tested compounds within this study show some characteristic differences, with signal "bulges" superimposed over the typical 1/*f* curve profile.

Table 1 Performance metrics derived from different measurement modalities applied to the tested volatile organic compounds, respective physical properties and Gutmann's donor–acceptor numbers[30]

VOC	I_{DS} max [μA]	Slope I_{DS}/V_{DS} [μA V^{-1}]	Mean AC [Ω]	ΔAC/Δf [mΩ Hz^{-1}]	ΔR_{DS} [Ω]	ΔR_{DS}/Δt [Ω s^{-1}]	ΔS_1 [×10^{-9}]	ΔS_2 [×10^{-9}]	ΔS_3 [×10^{-9}]	Boiling point [°C]	Vapour pressure [kPa @ 25 °C]	DN	AN	DN – AN
Water	179	893	945	2.9	−28	−0.18	1330	337	202	100	3.17	18.0	54.8	−36.8
Methanol	209	1043	1043	3.3	−21	−0.28	647	348	205	64.7	13.02	19.0	41.5	−22.5
Acetonitrile	186	930	941	3.3	−15	−0.17	1244	276	197	82	9.71	14.1	18.9	−4.8
Acetone	169	844	1009	2.3	10	0.14	408	340	231	56	30.6	17.0	12.5	+4.5
Ethanol	173	867	978	2.4	−8	−0.1	799	380	211	78.4	5.95	19.2	37.9	−18.7
Diethyl ether	228	1138	728	1.8	−4	−0.05	873	350	228	34.6	58.66	19.2	3.9	+15.3
Dichloromethane	227	1136	947	2.8	−12	−0.41	984	455	341	39.6	57.3	1.0	20.4	−19.4
Heptane	189	947	1151	3.2	1	0.004	736	422	261	98.4	5.33	0	0	0
THF	172	859	1288	3.4	25	0.22	309	310	215	66	17	20.0	8.0	+12.0
Chloroform	192	959	880	2.2	−35	−0.46	1243	451	360	61.2	25.9	4.0	23.1	−19.1
Decane	215	1076	1006	3.0	−30	−0.37	599	316	197	174.1	0.17	N/A	N/A	N/A
Isoprene	220	1098	755	2.5	−10	−0.06	1215	375	248	34.1	53.2	N/A	N/A	N/A
Styrene	215	1077	770	2.7	−24	−0.34	871	370	236	145	0.67	5.0	N/A	N/A
Hexaldehyde	211	1053	774	2.4	−20	−0.09	372	323	235	129	1.33	16.0	N/A	N/A
Limonene	227	1135	726	2.4	−12	−0.09	880	471	242	176	0.202	N/A	N/A	N/A
NMP	196	978	861	2.1	32	0.31	830	257	202	202	0.05	27.3	13.3	+14.0

N/A – not available. 🟩 – correct classification. 🟥 – incorrect classification.

In order to distinguish these traces even more, we decided to subtract from them the spectral noise profile of nitrogen (present in Fig. S2d†), thereby obtaining the graphs in Fig. 4a and b. Distinctive characteristics between the tested VOCs can be readily identified by spectral bands including the predominance of the traces for the compounds containing –Cl atoms (dichloromethane and chloroform) in the spectrum > 100 Hz (higher noise level); the appearance of a positive "bulge" in the band between 10 and 20 Hz for VOCs whose chemical structure contains a ring of atoms or aromatic structures (limonene, styrene and THF); a negative "bulge" centred at around 2–10 Hz for compounds with a high number of composing atoms disposed on a single linear structure such as decane, hexaldehyde, and diethyl ether; and for VOCs with low molecular weights, such as methanol, ethanol and acetone, following a similar profile to water.

By applying spectral signal separation or decomposition by means of filter-bank analysis, the differences mentioned above can be better quantified and visualized. With the view of achieving this, a recursive filter-bank algorithm was developed and applied to the acquired spectral noise signals, whose mathematical formulation is,[39]

$$M_0 = \{\Delta S_n / I \times \text{freq}\} \otimes h_{\text{LP}} \tag{1}$$

$$M_n = M_{n-1} \otimes h_{\text{LP}} \tag{2}$$

$$h_{\text{LP}} = 1/8[(1+\sqrt{3})(3+\sqrt{3})(3-\sqrt{3})(1-\sqrt{3})] \tag{3}$$

where M_n and M_{n-1} represent the output of the filter bank for components n and $n-1$, respectively, after convolution with h_{LP}. The coefficients of this low-pass filter are based on the four Daubechies coefficients, which produce sub-band signals that are orthogonal to each other, commonly applied in the fields of signal and image processing involving filter analysis and synthesis (such as wavelet transforms and filter banks). In total, 6 spectral components (M_0 to M_5) were extracted from the differential spectral noise traces, with examples of these components shown in Fig. 4c and d for heptane and limonene, respectively. From the exemplary traces, signal differences for M_0 and M_1 components can be detected for nominal frequencies < 0.1 (sub-band S_1), as well as different curve slopes between frequency bands of 0.1 and 0.4 (M_0 through M_5, sub-band S_2), and an increased number of peaks (and respective amplitude) towards the end of the spectrum (frequencies > 0.4, sub-band S_3), especially for components M_4 and M_5.

Quantification of these components involved the calculation of the cumulative sum of the spectrum (or noise power) along the three sub-bands denoted as ΔS_1, ΔS_2 and ΔS_3 in Table 1. A form of cross spectral noise correlation was afterwards performed where the spectral components from different VOCs were grouped in pairs and the sum of the differences between peak intensities (maximum amplitude) inside each sub-band were calculated, thus providing the complete correlation matrix in the form of a 2D distribution map as shown in Fig. 4e. By its turn, based on the location of the maximum peak intensity for the three sub-bands in every spec-

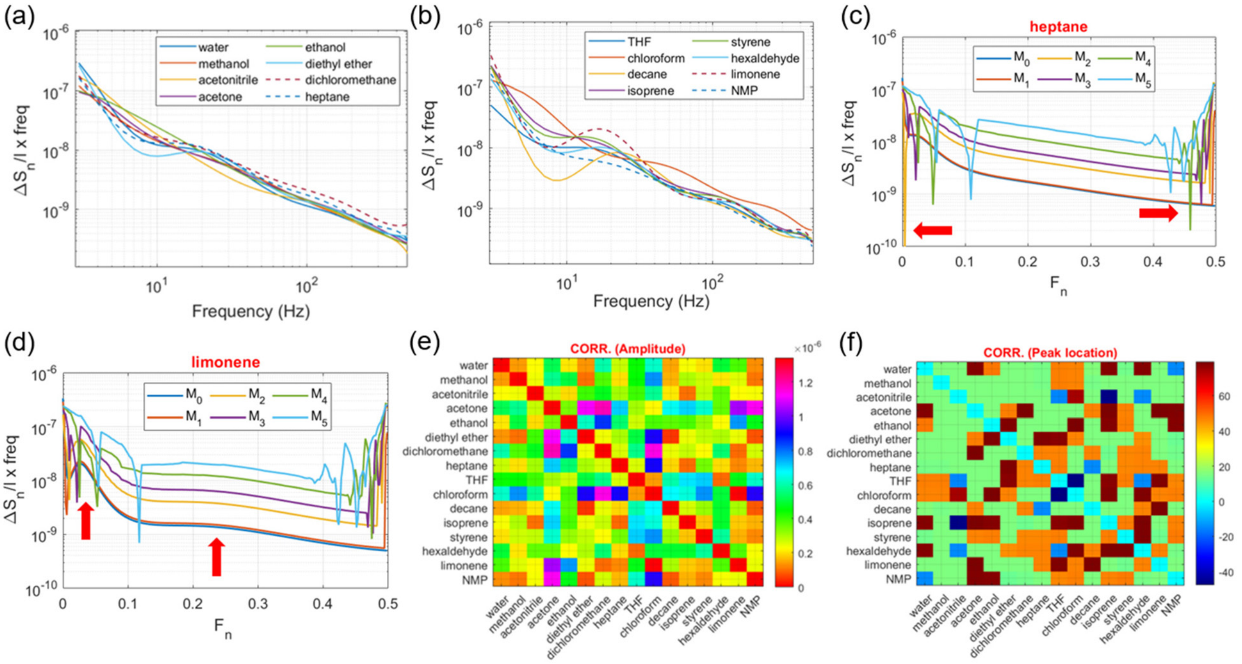

Fig. 4 (a) and (b) Differential spectral noise obtained for the tested VOCs by subtraction with the spectral noise measured for nitrogen. (c) Spectral components (M_0 to M_5) obtained after the application of the filter bank to the differential noise measured for heptane. (d) Similar spectral components obtained for limonene. Note: the red arrows mark some visual differences between the traces of the spectral components for heptane and limonene. (e) Correlation matrix for the tested VOCs in terms of the sum of the differences in peak intensity measured for different spectral components. (f) Similar correlation matrix calculated in terms of the average difference in peak location measured for M_0 to M_5.

tral component (M_0 to M_5), a new cross-correlation matrix was calculated that uses the average difference between peak locations in S_1, S_2 and S_3 during the VOC pairing comparison (Fig. 4f). From the previous figures, the average difference in the peak location is within 20 Hz and the sum of intensity differences is around 0.5×10^{-6}.

Finally, Table 1 presents quantified performance metrics calculated for the VOC signals obtained by the different measurement modalities present in the current study, in conjunction with some physical properties, namely boiling temperature, vapour pressure, and the donor–acceptor numbers derived from Gutmann's theory, which are used to further identify characteristic patterns amongst the compounds. Notably, the $\Delta AC/\Delta f$ metric (variation of AC impedance with frequency) shows very close values between the VOCs (mean: 2.67 ± 0.48 mΩ Hz^{-1}) and above the value obtained for graphene under open-air conditions (1.6 mΩ Hz^{-1}), thus reflecting the interaction produced by gas molecules on the graphene channel, from which heptane presents lower performance metrics in general (ΔR_{DS}, $\Delta R_{DS}/\Delta t$, DN − AN), followed by diethyl ether and isoprene, the latter ones exhibiting the highest vapour pressure levels under the experimental conditions. Interestingly, some slightly polar molecules tested in this study like dichloromethane showed a lower resistance variation recorded overtime as compared to other non-polar molecules (*e.g.*, decane), though other GFET metrics, namely the rate of resistance change ($\Delta R_{DS}/\Delta t$), clearly show higher values (in modulus) for dichloromethane and chloroform. In face of these results, we postulate that due to the geometrical arrangement of the atoms along the dichloromethane molecule (that is, between two Cl and H atoms), it tends to create different spatial arrangements or orientations relative to the planar layout of graphene that lowers the measured resistance variation overtime after the initial fast drop (Fig. 3b). By its turn, ΔS_3 is clearly higher for compounds with –Cl groups, whereas the ratio $\Delta S_1/\Delta S_2$ is closer to 2 for compounds such as limonene, styrene and decane, both characterized by a high number of carbon atoms in their structure and, for whom, the classification in terms of donor–acceptor species is difficult to estimate (not available in the literature). At the end, the original division of the 16 tested VOCs into 6 different groups based on chemical structure similarity (Fig. 4a) does not translate into similar GFET metrics, as compounds within the same original group (such as ethanol and acetone) can produce different resistance variations and noise levels in graphene, with many of these discrepancies being explained in here by resorting to the donor–acceptor theory and/or spectral signatures within specific frequency bands. Therefore, the original division in Fig. 4a should only be regarded as a tentative separation of these compounds before GFET experimentation.

Conclusions

The present manuscript has presented a GFET device involved in the detection of different VOC vapours in nitrogen carrying gas medium, which can be used as medically relevant biomarkers for diseases affecting the respiratory, endocrine, gastrointestinal, circulatory, or neurological body systems and expelled through breath condensate. The availability of 12 independent graphene channels connected to a multiplexed readout system allowed the testing of different signal modalities, including cyclic time measurements for the variation of graphene's resistance in DC and AC regimes, as well as the low-frequency spectral noise, both used in the identification of specific spectral signatures related to chemical structures present within the tested VOCs, with additional compound separation following the principles of donor–acceptor species derived from Gutmann's theory. The use of more distinct measurement modalities also reflected the fact that under the conditions of the experiment, no gating signal was applied to the GFET chip array and, thus no transfer characteristic curve could be obtained for the tested VOCs. Since the employed GFET chip array only allowed for reliable top-gating stimulation (instead of back-gating), a physical conductive path between the gate and the graphene channels could not be established by the vapour molecules in an unbound gaseous state.

Although we opted to conduct gas experiments closer to homeostatic physiological conditions, wherein some of the tested VOCs might not reach enough vapour pressures to induce strong interactions with graphene (as reported in other literature studies), our proposed system was still able to detect spectral and time signatures unique to certain compounds. Since modern E-nose devices still rely massively on pattern recognition to identify and separate chemical species, the extracted data from the current study can also be included in the portfolio of such algorithms for future point-of-care healthcare devices. Apart from the potential diagnostic capability of the proposed device, we are aware that more testing is required to assess its reliability, namely by using gas mixtures with more than a single VOC, as well as working even closer to realistic gas exchange conditions from body tissues. Under such conditions, the limit-of-detection for each VOC can be better estimated by the proposed VOC detection system (and conformed to a patient-dependent breath exhalation rate) as the electrical performance of the device still allows resolution increments for the different measurement modalities.

Author contributions

Conceptualization and investigation: B. G., D. W. and H. T. Data curation and visualization: B. G. and D. W. Writing – original draft: B. G. Writing – review and editing: D. W., H. T. and E. Y. Project administration and funding: E. Y.

Conflicts of interest

There are no conflicts to declare.

Acknowledgements

The authors acknowledge the Engineering and Physical Sciences Research Council (EPSRC) in the United Kingdom for the grant "EP/P012779".

References

1 W. Fu, L. Jiang, E. P. van Geest, L. M. C. Lima and G. F. Schneider, Sensing at the surface of graphene field-effect transistors, *Adv. Mater.*, 2016, **29**, 6.
2 C. Mackin, E. McVay and T. Palacios, Frequency response of graphene electrolyte-gated field-effect transistors, *Sensors*, 2018, **18**, 494.
3 S. S. Sekhon, P. Kaur, Y.-H. Kim and S. S. Sekhon, 2D graphene oxide-aptamer conjugate materials for cancer diagnosis, *npj 2D Mater. Appl.*, 2021, **5**, 21, DOI: 10.1038/s41699-021-00202-7.
4 B. Gil, S. Anastasova and B. Lo, Graphene field-effect transistors array for detection of liquid conductivities in the physiological range through novel time-multiplexed impedance measurements, *Carbon*, 2022, **193**, 394.
5 E. Singh, M. Meyyappan and H. S. Nalwa, Flexible graphene-based wearable gas and chemical sensors, *ACS Appl. Mater. Interfaces*, 2017, **9**, 34544.
6 B. Li, H. Tan, D. Jenkins, V. S. Raghavan, B. G. Rosa, F. Guder, G. Pan, E. Yeatman and D. J. Sharp, Clinical detection of neurodegenerative blood biomarkers using graphene immunosensor, *Carbon*, 2020, **168**, 144.
7 H. Tan, Y. Fan, Y. Rong, B. Porter, C. S. Lau, Y. Zhou, Z. He, S. Wang, H. Bhaskaran and J. H. Warner, Doping graphene transistors using vertical stacked monolayer WS_2 heterostructures grown by chemical vapor deposition, *ACS Appl. Mater. Interfaces*, 2016, **8**, 1644.
8 M. Biabanifard, A. Arsanjani, M. S. Abrishamian and D. Abbott, Tunable terahertz graphene-based absorber design method based on a circuit model approach, *IEEE Access*, 2020, **8**, 70343.
9 M. A. Brown, M. S. Crosser, M. R. Leyden, Y. Qi and E. D. Minot, Measurement of high carrier mobility in graphene in an aqueous electrolyte environment, *Appl. Phys. Lett.*, 2016, **109**, 093104.
10 J. Xia, F. Chen, J. Li and N. Tao, Measurement of the quantum capacitance of graphene, *Nat. Nanotechnol.*, 2009, **4**, 505.
11 C.-F. Chen, C.-M. Park, B. W. Boudouris, J. Horne, B. Gong, C. Girit, A. Zettl, M. F. Crommie, R. A. Segalman, S. G. Louie and F. Wang, Controlling inelastic light scattering quantum pathways in graphene, *Nature*, 2011, **471**, 617.
12 J. Liu, Q. Li, Y. Zou, Q. Qian, Y. Jin, G. Li, K. Jiang and S. Fan, The dependence of graphene Raman D-band on carrier density, *Nano Lett.*, 2013, **13**, 6170.
13 S. Cheng, S. Hideshima, S. Kuroiwa, T. Nakanishi and T. Osaka, Label-free detection of tumour markers using

field effect transistor (FET)-based biosensors for lung cancer diagnosis, *Sens. Actuators, B*, 2015, **212**, 329.

14 I. Novodchuk, M. Bajcsy and M. Yavuz, Graphene-based field effect transistor biosensors for breast cancer detection: a review on biosensing strategies, *Carbon*, 2021, **172**, 431.

15 Y. Kanai, J. O. Matsuyama, M. Tanioku, S. Ushiba, T. Ono, K. Ioue, T. Kitaguchi, M. Kimura, H. Ueda and K. Matsumoto, Graphene field effect transistor-based immunosensor for ultrasensitive non-competitive detection of small antigens, *ACS Sens.*, 2020, **5**, 24.

16 T. Yin, L. Xu, B. Gil, N. Merali, M. S. Sokolikova, D. C. A. Gaboriau, D. S. K. Liu, A. Nizamuddin, M. Mustafa, S. Alodan, M. Chen, O. Txoperena, M. Arrastua, J. M. Gomez, N. Ontoso, M. Elicegui, E. Torres, D. Li, C. Matteui, A. E. Frampton, L. R. Jiao, S. Ramadan and N. Klein, Graphene sensor arrays for rapid and accurate detection of pancreatic cancer exosomes in patients' blood plasma samples, *ACS Nano*, 2023, **17**, 14619–14631.

17 L. Xu, S. Ramadan, B. G. Rosa, Y. Zhang, T. Yin, E. Torres, O. Shaforost, A. Panagiotopoulos, B. Li, G. Kerherve, D. K. Kim, C. Mattevi, L. R. Jiao, P. K. Petrov and N. Klein, On-chip integrated graphene aptasensor with portable readout for fast and label-free COVID-19 detection in virus transport medium, *Sens. Diagn.*, 2022, **1**, 719.

18 H. Liu, Y. Liu, Y. Chu, T. Hayasaka, N. Joshi, Y. Cui, X. Wang, Z. You and L. Lin, AC phase sensing of graphene FETs for chemical vapors with fast recovery and minimal baseline drift, *Sens. Actuators, B*, 2018, **263**, 94.

19 S. Rumayantsev, G. Liu, M. S. Shur, R. A. Potyrailo and A. A. Balandin, Selective gas sensing with a single pristine graphene transistor, *Nano Lett.*, 2012, **12**, 2294.

20 W. M. Ahmed, O. Lawal, T. M. Nijen, R. Goodacre and S. J. Fowler, Exhaled volatile organic compounds of infection: a systemic review, *ACS Infect. Dis.*, 2017, **3**, 695.

21 W. Ibrahim, L. Carr, R. Cordell, M. J. Wilde, D. Salman, P. S. Monks, P. Thomas, C. E. Brightling, S. Siddiqui and N. J. Greening, Breathomics for the clinician: the use of volatile organic compounds in respiratory diseases, *Thorax*, 2021, **76**, 514.

22 J. E. Belizario, J. Faintuch and M. G. Malpartida, Breath biopsy and discovery of exclusive volatile organic compounds for diagnosis of infectious diseases, *Front. Cell. Infect. Microbiol.*, 2021, **10**, 564194.

23 A. J. Li, V. K. Pal and K. Kannan, A review of environmental occurrence, toxicity, biotransformation and biomonitoring of volatile organic compounds, *Environ. Toxicol. Chem.*, 2021, **3**, 91.

24 J. O. Ogbodo, A. V. Arazu, T. C. Iguh, N. J. Onwodi and T. C. Ezike, Volatile organic compounds: a proinflammatory activator in autoimmune diseases, *Front. Immunol.*, 2022, **13**, 928379.

25 F. Buljubasic and G. Buchbauer, The scent of human diseases: a review on specific volatile organic compounds as diagnostic biomarkers, *Flavour Fragrance J.*, 2015, **30**, 2.

26 S. Sethi, R. Nanda and T. Chakraborty, Clinical application of volatile organic compound analysis for detecting infectious diseases, *Clin. Microbiol. Rev.*, 2013, **26**, 463.

27 C. Course, W. J. Watkins, C. T. Muller, D. Odd, S. Kotecha and M. Chakraborty, Volatile organic compounds as disease predictors in newborn infants: a systematic review, *J. Breath Res.*, 2021, **15**, 024002.

28 T. Hayasaka, A. Lin, V. C. Copa, L. P. Lopez, R. A. Loberternos, L. I. M. Ballesteros, Y. Kubota, Y. Liu, A. A. Salvador and L. Lin, An electronic nose using a single graphene FET and machine learning for water, methanol, and ethanol, *Microsyst. Nanoeng.*, 2020, **6**, 50.

29 A. A. Balandin, Low-frequency 1/f noise in graphene devices, *Nat. Nanotechnol.*, 2013, **8**, 549.

30 V. Gutmann, Empirical parameters for donor and acceptor properties of solvents, *Electrochim. Acta*, 1976, **21**, 661.

31 M. Schmeisser, P. Illner, R. Puchta, A. Zahl and R. van Eldik, Gutmann donor and acceptor numbers for ionic liquids, *Chem. – Eur. J.*, 2012, **18**, 10969.

32 N. Alzate-Carvajal, J. Park, I. Bargaoui, R. Rautela, Z. J. Comeau, L. Scarfe, J.-M. Menard, S. B. Darling, B. H. Lessard and A. Luican-Mayer, Arrays of functionalized graphene chemiresistors for selective sensing of volatile organic compounds, *ACS Appl. Electron. Mater.*, 2023, **5**, 1514–1520.

33 A. Lipatov, A. Varezhnikov, P. Wilson, V. Sysoev, A. Kolmakov and A. Sinitskii, Highly selective gas sensor arrays based on thermally reduced graphene oxide, *Nanoscale*, 2013, **5**, 5426–5434.

34 X. Yan, Y. Wu, R. Li, C. Shi, R. Moro, Y. Ma and L. Ma, High performance UV-assisted NO_2 sensor based on chemical vapor deposition of graphene at room temperature, *ACS Omega*, 2019, **4**, 14179–14187.

35 N. Alzate-Carvajal and A. Luican-Mayer, Functionalized graphene surfaces for selective gas sensing, *ACS Omega*, 2020, **5**, 21320–21329.

36 C. Mackin, V. Schroeder, A. Zurutuza, C. Su, J. Kong, T. M. Swager and T. Palacios, Chemiresistive graphene sensors for ammonia detection, *ACS Appl. Mater. Interfaces*, 2018, **10**, 16169–16176.

37 T. Rungreungthanapol, C. Homma, K.-I. Akagi, M. Tanaka, J. Kikuchi, H. Tomizawa, Y. Sugizaki, A. Isobayashi, Y. Hayamizu and M. Okochi, Volatile organic compound detection by graphene field-effect transistors functionalized with fly olfactory receptor mimetic paptides, *Anal. Chem.*, 2023, **95**, 4556–4563.

38 S. Grimnes and O. G. Martinsen, *Bioimpedance and bioelectronics basics*, Elsevier Ltd., Amsterdam, The Netherlands, 2nd edn, 2008.

39 B. M. G. Rosa and G.-Z. Yang, A flexible wearable device for measurement of cardiac, electrodermal, and motion parameters in mental healthcare applications, *IEEE J. Biomed. Health Inform.*, 2019, **23**, 2276.